Local-field and excitonic effects in the optical response of α-alumina

A. G. Marinopoulos[1] and Myrta Grüning[2,3]

[1]*CEMDRX and Physics Department, University of Coimbra, Rua Larga 3004-516 Coimbra, Portugal*

[2]*Centre for Computational Physics and Physics Department, University of Coimbra, Rua Larga 3004-516 Coimbra, Portugal*

[3]*European Theoretical Spectroscopy Facility, NAPS/IMCN, Université Catholique de Louvain, B-1348 Louvain-la Neuve, Belgium*

(Received 15 February 2011; revised manuscript received 18 March 2011; published 25 May 2011)

This paper introduces key ingredients of the dielectric response of α-alumina that go beyond an independent-particle (IP) treatment of the valence-electron excitations. The optical-response functions were calculated from first- principles both at the Bethe–Salpeter and the random-phase approximation (RPA) levels. Excitonic effects obtained within the Bethe–Salpeter framework were found essential for reproducing the low-energy part of the experimental spectra (below 15 eV) and the bound exciton in particular. For higher energies, local-field effects introduced through the RPA modified considerably the IP results and provided a satisfactory account of the reflectivity spectra and of the position and shape of the dominant bulk plasmon resonance in the electron energy-loss spectra.

DOI: 10.1103/PhysRevB.83.195129 PACS number(s): 71.15.Qe, 71.35.−y, 78.20.Ci, 78.66.Nk

I. INTRODUCTION

α-alumina (α-Al_2O_3) is a wide band-gap insulator and an important structural ceramic with diverse uses, for instance, as an abrasive, a component in cutting tools, a catalyst and catalyst support, and an optical material.[1] Its electronic band structure and excitations have been studied by a variety of experimental techniques including optical,[2–9] x-ray emission,[10,11] photoelectron,[11] and electron energy-loss[9,12] spectroscopies. The most detailed studies of the valence-electron excitations and optical response have been performed by means of vacuum ultraviolet (VUV) spectroscopy.[3–5,7–9] This specific technique allowed the complete coverage of the energy range of the interband transitions, offering at the same time a superior energy resolution. The anisotropy of the optical response of α-alumina, a uniaxial solid with the hexagonal (0001) basal planes stacked parallel to the crystallographic c axis, was also investigated by making use of polarized light from synchrotron-radiation light sources providing the reflectivity spectra for polarizations parallel and perpendicular to the hexagonal c axis.[5] In these studies the VUV reflectivity spectra for sufficiently low temperatures displayed a strong excitonic peak at about 9 eV. By studying the dependence of the optical reflectivity with temperature, the exciton binding energy was estimated to be 0.13 eV.[7]

Theoretically, both semiempirical[13–16] and first-principles[17–19] schemes based on density-functional theory (DFT)[20,21] have been employed to determine the electronic band structure of α-alumina. Concerning the optical response and related dielectric functions, the existing first-principles calculations[18,19,22,23] are based on an independent-particle (IP) treatment of the electronic excitations, where the latter are described solely by noninteracting electron-hole pairs.[24] The electron quasiparticle (QP) energies in these studies were approximated by the Kohn–Sham energies as determined by a self-consistent determination of the ground state within the DFT. Despite the fact that these calculations reproduced reasonably well the salient features of the measured optical spectra,[18,19,22,23] they relied on an *ad hoc* shift of the spectra (by 2 eV) toward higher energies and invariably failed to predict the steep onset of oscillator strength, leading to the strong exciton peak just above the absorption edge.

In this paper we have calculated the optical response of α-alumina beyond the IP level of approximation: We included self-energy corrections to the electron QP energies, local-field effects (LFEs), and the electron-hole attraction, which is the origin of excitonic effects in solids. On one hand we treated the QP corrections and the electron-hole interaction within the GW approximation[25,26] and Bethe–Salpeter (BS) equation[24,27] frameworks, respectively. On the other hand we included just LFEs within the random-phase approximation (RPA).[28] The methodologies of both schemes are presented in Sec. II. The former scheme is certainly more accurate, incorporating many-body effects in the electron response, but its computational cost allowed us to calculate only a restricted part of the excitation spectra, whereas the RPA can cover a much larger energy range and has already given reliable energy-loss spectra for solids.[29,30] In Sec. III we initially discuss the effect of the QP corrections to the DFT band structure. Our results (Sec. III) show that LFEs and electron-hole attraction are both important, though in different energy regions, and describe satisfactorily the experimental spectra. We compare first the results for the reflectivity spectra (Sec. III B)–directly obtained from experiment—and then the results for a number of dielectric-response functions (Sec. III C): the macroscopic dielectric function, index of refraction, extinction coefficient, and energy-loss function, which for this material are commonly accessed experimentally through Kramers–Kronig analyses of the measured reflectivity and energy-loss data. Finally, in Sec. IV we discuss the relative importance of many-body effects in specific energy regions and present our concluding remarks.

II. METHODOLOGICAL BACKGROUND

A. Calculation of the macroscopic dielectric function

The frequency-dependent macroscopic dielectric function, ϵ_M, is the principal quantity needed for the calculation of the optical and dielectric functions of solids.[24] We calculated ϵ_M at two levels of approximation: at the RPA level[28] and at the BS

level.[24,27] In both cases, we started from the IP eigenfunctions and eigenenergies $\{\psi^0_{n\mathbf{k}},\varepsilon^0_{n\mathbf{k}}\}$ (n being the band index, and $\mathbf{k}$ the generic vector of the grid sampling of the Brillouin zone) calculated at the Kohn–Sham[21] DFT level.[20]

Within the RPA, the microscopic dielectric function ϵ in the reciprocal space for a periodic system and for a wave vector $\mathbf{q}$ is given by

$$\epsilon_{\mathbf{GG}'}(\mathbf{q},\omega) = \delta_{\mathbf{GG}'} - v(\mathbf{q}+\mathbf{G})\,\chi^0_{\mathbf{GG}'}(\mathbf{q},\omega), \tag{1}$$

with $\mathbf{G}$ and $\mathbf{G}'$ being the reciprocal lattice vectors. v is the bare Coulomb interaction and χ^0 is the noninteracting response function calculated from the DFT eigenfunctions and eigenenergies.[24] The ϵ_M is obtained using its definition in terms of the inverse of ϵ,[31]

$$\epsilon_M(\omega) = \lim_{\mathbf{q}\to 0} \frac{1}{[\epsilon(\mathbf{q},\omega)^{-1}]_{\mathbf{G}=0\,\mathbf{G}'=0}}. \tag{2}$$

When ϵ in Eq. (1) is diagonal, Eq. (2) reduces to a simple macroscopic average and corresponds to the IP treatment of excitations. Instead, by considering ϵ as a matrix in the space of reciprocal vectors, and including the off-diagonal elements in the matrix inversion, we effectively include the effects of microscopic fields—the LFE—that locally counteract the effect of the external field.

Within the BS framework, correlation effects beyond the IP approximation are taken into account. First, the self-energy-corrected QP energies are used instead of the DFT energies, and second, the electron-hole interaction is included in the description of the excited states. The QP corrections are calculated within the GW approximation.[25,26] Within this approach the QP energy $E^{\mathrm{QP}}_{n\mathbf{k}}$ is calculated by adding to the corresponding DFT eigenenergy $\varepsilon^0_{n\mathbf{k}}$ the first-order perturbation correction that comes from replacing the DFT exchange-correlation potential v_{xc} with the GW self-energy operator Σ_{GW}:

$$E^{\mathrm{QP}}_{n\mathbf{k}} = \varepsilon^0_{n\mathbf{k}} + \Re\left\{Z_{n\mathbf{k}}\left\langle\psi^0_{n\mathbf{k}}\right|\Sigma_{GW} - v_{\mathrm{xc}}\left|\psi^0_{n\mathbf{k}}\right\rangle\right\}. \tag{3}$$

The renormalization factor Z accounts for the fact that Σ_{GW}, which is energy dependent, should be evaluated at $E^{\mathrm{QP}}_{n\mathbf{k}}$. The GW self-energy operator Σ_{GW} is the convolution in frequency space between the noninteracting one-electron Green's function G and the screened Coulomb potential W. The screening in W is described by a dielectric function ϵ that was calculated within the RPA with a frequency dependence approximated by a plasmon-pole model.[32]

Electron-hole interaction is introduced at the BS level,[27] by solving the eigenvalue problem for the two-particle Hamiltonian H,[24]

$$H_{\substack{nn'\mathbf{k}\\ mm'\mathbf{k}'}} = \left(E^{\mathrm{QP}}_{n\mathbf{k}} - E^{\mathrm{QP}}_{n'\mathbf{k}}\right)\delta_{nm}\delta_{n'm'}\delta_{\mathbf{kk}'} + (f_{n'\mathbf{k}} - f_{n\mathbf{k}})\,\Xi_{\substack{nn'\mathbf{k}\\ mm'\mathbf{k}'}}, \tag{4}$$

where $f_{n\mathbf{k}}$ are the occupation factors, and the matrix $\Xi_{\substack{nn'\mathbf{k}\\ ss'\mathbf{k}_1}} = 2\bar{V}_{\substack{nn'\mathbf{k}\\ ss'\mathbf{k}_1}} - W_{\substack{nn'\mathbf{k}\\ ss'\mathbf{k}_1}}$ is the BS kernel containing a bare Coulomb interaction term $\bar{V}$, and a screened electron-hole interaction term W. On a finite grid of transferred momenta $\mathbf{q}$, $\bar{V}$ and W read

$$\bar{V}_{\substack{nn'\mathbf{k}\\ ss'\mathbf{k}_1}} = \frac{1}{\Omega N_q}\sum_{\mathbf{G}\neq 0}\rho_{nn'\mathbf{k}}(\mathbf{q}=0,\mathbf{G}) \times\rho^*_{ss'\mathbf{k}_1}(\mathbf{q}=0,\mathbf{G})\,v(\mathbf{G}), \tag{5}$$

$$W_{\substack{nn'\mathbf{k}\\ ss'\mathbf{k}_1}} = \frac{1}{\Omega N_q}\sum_{\mathbf{GG}'}\rho_{ns\mathbf{k}}(\mathbf{q}=\mathbf{k}-\mathbf{k}_1,\mathbf{G}) \times\rho^*_{n's'\mathbf{k}_1}(\mathbf{q}=\mathbf{k}-\mathbf{k}_1,\mathbf{G}')\epsilon^{-1}_{\mathbf{GG}'}v(\mathbf{q}+\mathbf{G}'). \tag{6}$$

where $\rho_{nm\mathbf{k}}(\mathbf{q},\mathbf{G}) = \langle\psi^0_{n\mathbf{k}}|e^{i(\mathbf{q}+\mathbf{G})\cdot\mathbf{r}}|\psi^0_{m\mathbf{k}-\mathbf{q}}\rangle$, Ω is the unit cell volume, and N_q is the number of transferred momenta. $\bar{V}$ stems from the density variation of the Hartree part and takes into account LFEs (setting $\Xi = 2\bar{V}$ corresponds to the RPA). W comes from the variation of the self-energy and takes into account the electron-hole attraction. While the latter term is frequency dependent, we used, as it is generally done, a static approximation. The eigenvalues E_λ and eigenvectors $A^\lambda_{n'n\mathbf{k}}$ of Eq. (4), are finally used to calculate ϵ_M as

$$\epsilon_M(\omega) = 1 - \lim_{\mathbf{q}\to 0}\frac{8\pi}{|\mathbf{q}|^2\Omega N_q}\sum_{nn'\mathbf{k}}\sum_{mm'\mathbf{k}'}\rho^*_{n'n\mathbf{k}}(\mathbf{q},\mathbf{G}) \times\rho_{m'm\mathbf{k}'}(\mathbf{q},\mathbf{G}')\sum_\lambda\frac{A^\lambda_{n'n\mathbf{k}}\left(A^\lambda_{m'm\mathbf{k}'}\right)^*}{\omega - E_\lambda}, \tag{7}$$

The eigenvalue problem [Eq. (4)] was solved iteratively using the Lanczos–Haydock approach for the full non-Hermitian matrix as proposed in Ref. 33. In fact, considering the full Hamiltonian, and not only its resonant part as is usually done, was found necessary in the present study for calculating the reflectivity, the energy-loss function,[34] and all dielectric functions that contain the real part, ϵ_1, of ϵ_M.

B. Computational details

The Kohn–Sham energy eigenvalues and wave functions and structural parameters of α-alumina were determined within the DFT using the local-density approximation[35] (LDA) for exchange and correlation. The calculations were carried out with the ABINIT code.[36–38] The crystalline wave functions were expanded on a plane-wave basis set up to kinetic energy cutoff of 35 Ha and norm-conserving Troullier–Martins pseudopotentials were employed.[39] A Monkhorst–Pack[40] 4×4×4 mesh was selected for the Brillouin-zone (BZ) integrations. Maximally localized wave functions (MLWFs) were obtained using the WANNIER90[41] interface in ABINIT.

The GW calculations for the QP corrections and the RPA and BS calculations for the macroscopic dielectric matrix were performed using the YAMBO code.[42] The self-energy Σ_{GW} in Eq. (3) was evaluated at the Kohn–Sham energies $\varepsilon^0_{n\mathbf{k}}$. For the QP corrections, we included 200 bands in the Green's function and 580 bands and 629 reciprocal lattice vectors in the dielectric matrix. With these parameters the band-gap correction converged to within 0.1 eV. To obtain converged spectra and functions at the RPA level spanning a range of up to 42 eV, we included 160 bands and 223 reciprocal lattice vectors when calculating the response function χ^0 in Eq. (1).

For the BS calculations, the BZ was sampled with a $11\times11\times11$ Monkhorst–Pack grid giving 1331 points in the full BZ. The BS equation was solved by taking a basis consisting of 12 of the upper valence and 12 of the lower conduction bands, but limiting the electron-hole energy range to 18.7 eV. For calculating the static screening in W we included 168 bands and 121 reciprocal lattice vectors. Finally, to calculate the electron-hole exchange and electron-hole attraction matrices we included 223 and 25 reciprocal vectors, respectively. The above parameters, and in particular the choice for the basis, ensured converged BS spectra up to 13.5 eV, but at the same time limited the validity of the BS results for providing converged values at low energies (below 7 eV) for the real part of ϵ_M, ϵ_1, and for the functions containing ϵ_1.

III. RESULTS

A. Equilibrium geometry and electronic band structure

The hexagonal α phase of alumina is described by a trigonal (rhombohedral) space group ($R\bar{3}c$, no. 137) with 10 atoms (4 Al and 6 O) in the primitive unit cell. From the geometry optimization we obtained 5.05 Å for the lattice parameter and 55.32° for the rhombohedral angle, in close agreement with previous DFT-LDA results[43,44] and the existing experimental data.[45]

Figure 1 shows the calculated DFT band structure along high-symmetry directions in the first BZ. The valence-band edge was taken as the energy zero. The valence bands consist of two well-separated manifolds (labeled I and II starting from the lowest in energy). The corresponding MLWFs, reported in Fig. 2, allow us to identify their chemical character:[46] the lower manifold consisting of six bands located between −19 and −16 eV originates from the 2s states of the oxygens; the upper manifold consisting of 18 bands with a width of 7.25 eV originates instead from the 2p states of the oxygens with a mixed bonding and nonbonding character. In particular, the upper bands of manifold II exhibit very small dispersion and have probably a stronger nonbonding character than the lowermost more dispersing bands, which contain contributions from aluminum states.[18,19] The conduction bands consist of a single manifold with the lowest band exhibiting a strong

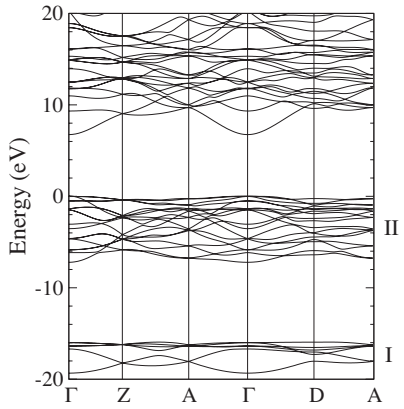

FIG. 1. DFT band structure of α-alumina within the LDA. The roman numbers label the valence manifolds.

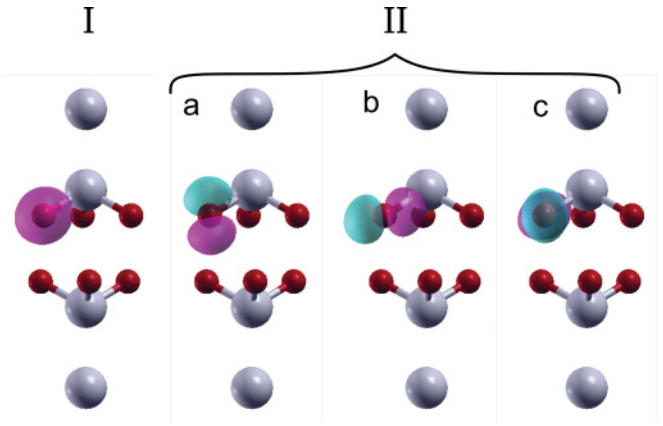

FIG. 2. (Color online) Isosurfaces of the MLWFs in α-alumina corresponding to the manifolds in Fig. 1: magenta and cyan indicate opposite isovalues. O atoms are in red, Al atoms in gray. Corresponding to manifold I there are six s-type MLWFs, each center at one of the six oxygens in the unit cell and slightly polarized toward the bonded Al. Corresponding to manifold II there are 18 p-type MLWFs pointing in three orthogonal directions (a,b,c) and centered at the six oxygens. For clarity only one MLWF per type is shown.

dispersion around the Γ point. From the LDA band structure we deduce a minimum direct band gap of 6.72 eV at Γ.

The magnitude of both the band gap and the upper manifold width are consistent with earlier DFT results at the LDA level.[19,22] Also the character of the valence bands from the Wannier functions analysis agrees with the previous analyses based on angular-momentum and site-projected densities of states.[18,19]

Figure 3 shows the QP corrections, as obtained within the GW approximation, plotted as a function of the energy of the LDA eigenvalues. The corrections shift the energy of the valence states toward more negative energies and raise the energy of conduction states having as total effect the opening of the valence-conduction band gap. The obtained QP corrections are not rigid in energy: we found that for

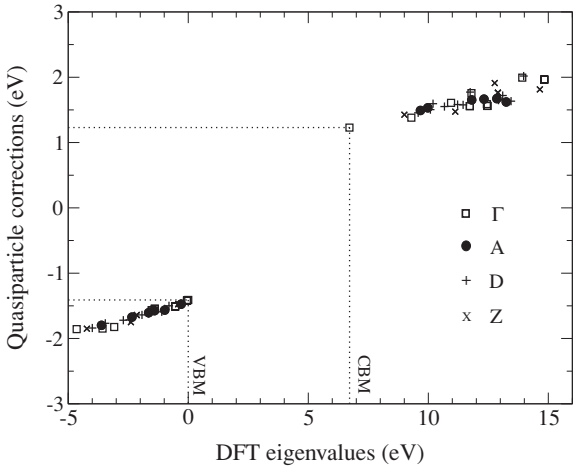

FIG. 3. QP corrections to the DFT eigenvalues for 12 valence and 12 conduction bands at high-symmetry points Γ (square), A (dot), D (plus), Z (x) in the first BZ. Dashed lines indicate the valence-band maximum (VBM) and conduction band minimum (CBM).

the energy region studied the corrections exhibit a linear dependence on the energy, which leads to a stretching of the bands with respect to the valence- and conduction-band edges, therefore increasing the LDA bandwidths. From a linear fit we found that the valence and conduction bands are stretched by about 11% and 8%, respectively.[47] At the Γ point the QP correction to the minimum gap amounts to 2.64 eV, giving a final QP gap of 9.36 eV, in excellent agreement with the experimental value of 9.4 eV[48] and slightly underestimated with respect to 9.57 eV deduced by French and co-workers from temperature-dependent VUV spectroscopy.[7]

Furthermore, by applying the stretching coefficient found by the linear fit of the valence states in Fig. 3 a width of 8.05 eV is obtained for the upper valence-band manifold (labeled II in Fig. 1) in agreement with the value measured by polarized x-ray emission spectroscopy (8 eV)[10] while smaller than the values of 9.2 and 9.5 eV obtained by photoelectron and soft x-ray emission spectroscopies.[11]

B. Reflectivity spectra

The existing experimental optical spectra on α-alumina are based on VUV reflectivity measurements[5,9] from which the dielectric response functions were obtained by Kramers–Kronig relations.[6] Using synchrotron radiation sources Tomiki and co-workers[5] measured reflectivity spectra up to 120 eV at 10 and 297 K for incident light parallel and perpendicular to the c axis. French and co-workers[9] measured reflectivity spectra at temperatures from 293 to 2167 K using a laser plasma light source and for light polarization perpendicular to the c axis.

The reflectivity R is related to the index of refraction n and extinction coefficient κ by

$$R = \frac{(n-1)^2 + \kappa^2}{(n+1)^2 + \kappa^2}, \tag{8}$$

which in turn are related to the real (ϵ_1) and imaginary (ϵ_2) parts of ϵ_M by

$$n = \frac{1}{\sqrt{2}}\left(\left(\epsilon_1^2 + \epsilon_2^2\right)^{1/2} + \epsilon_1\right)^{1/2} \tag{9}$$

$$\kappa = \frac{1}{\sqrt{2}}\left(\left(\epsilon_1^2 + \epsilon_2^2\right)^{1/2} - \epsilon_1\right)^{1/2}. \tag{10}$$

For analysis purposes we chose to discuss first our results for the reflectivity where a direct comparison to experimental data can be made. The results for the dielectric function ϵ_M, the index of refraction n, and extinction coefficient κ will be presented in the next subsection.

Figure 4 shows the reflectivity spectra for light polarizations (a) perpendicular and (b) parallel to the c axis calculated at the two levels of theory, RPA and BS, together with the measured VUV spectra obtained from the two different groups.[5,9] To elucidate the significance of LFEs and excitonic effects the spectra obtained at the IP level are also shown.

For both polarizations the experimental spectra display a sharp peak at 9.1 eV, appearing in a region of continuously increasing intensity. The subsequent increase in intensity eventually leads to two broader features centered around 13 and 20 eV. The latter has the largest intensity, reaching just above 30%. For higher energies the intensity decreases steadily until 30 eV, with a small rise in between 30 and 35 eV, most likely due to contributions coming from the deeper O(2s) bands.

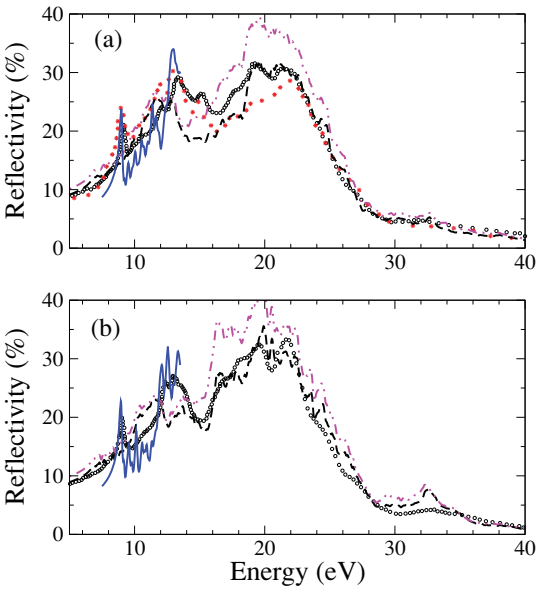

FIG. 4. (Color online) Reflectivity spectra for light polarizations (a) perpendicular and (b) parallel to the c axis: The calculated IP (magenta dotted-dashed), RPA (black dashed), and BS (solid blue) curves are compared with experimental data from Ref. 5 (black circles) and Ref. 9 (red stars).

The reflectivity spectra for the two different polarizations overall are similar, with some quantitative differences especially in the energy range between 10 and 18 eV. In this range a dip in reflectivity is seen for both polarizations, albeit at different energies (at 16 and 15 eV, for the perpendicular and parallel, respectively) that effectively splits the reflectivity spectra into two distinct regions. The spectrum for parallel polarization exhibits a more pronounced bimodal shape with the intensity dip falling below 20%. Also, in the spectrum for parallel polarization the features at about 13 eV are slightly red-shifted and have lower intensity and a different shape. For light polarization perpendicular to the c axis, the experimental spectra obtained from the two different groups generally agree, except in the intensity of the first peak at 9.1 eV and the shape of the feature centered at 20 eV.

Consistent with earlier calculations at the IP level,[19,22] the calculated IP spectra plotted in Fig. 4 are seen to provide a relatively good account of the experimental data for the higher energies, in this case for the part of the spectra after the reflectivity dip. The most notable difference at these energies is the intensity of the feature at 20 eV which is overestimated: The IP calculation predicts intensities between 35% and 40% instead of 30%. In contrast, at lower energies there are important differences: At energies below 9 eV the reflectivity intensity is slightly overestimated, the sharp peak at 9 eV is completely missing, and the feature centered at 13 eV is red-shifted by about 2 eV and underestimated in intensity.

The inclusion of LFEs through the RPA corrects some of the shortcomings of the IP results. At higher energies LFEs are particularly strong and reproduce remarkably well the experimental data for energies starting immediately after the intensity dip for either polarization by decreasing the overestimation of

the intensity obtained in the IP calculations. The agreement is very good in terms of the predicted intensity but also in terms of the line shape of the spectra. At low energies, LFEs correct the IP reflectivity intensity and reproduce accurately the low-frequency reflectivity limit measured experimentally for both light polarizations. Between 9 and 14 eV, LFEs are negligible and the agreement with experiment at the RPA level is as bad as at the IP level. Inclusion of QP corrections on top of the RPA would not improve the results. In fact the effect would be mostly a blue shift of about 2.6 eV that would worsen the comparison for energies below 9 eV and above 16 eV and not substantially improve in the intermediate region.

The part of the reflectivity spectra between 9 and 14 eV is well described only by including QP corrections together with electron-hole attraction at the BS level. The BS spectra show a sharp peak at about 9.0 eV, thus confirming its excitonic origin. The position of the peak is slightly lower in energy with respect to the experimental positions of 9.156 eV (perpendicular polarization) and 9.078 eV (parallel polarization) found at 10 K.[49] The broad feature at about 13 eV is also reasonably well reproduced as well as its dependence on the polarization. For perpendicular polarization two peaks can be distinguished at about 11.5 and 13.0 eV, and for parallel polarization three peaks at 12.1, 12.5, and 13.3 eV, in fairly good agreement with the experimental values: 12.12 and 13.42 eV for the perpendicular, and 12.45, 13.04, and 13.76 eV for the parallel polarization.[5]

C. Dielectric response functions

Figures 5 and 6 compare the ϵ_M calculated at the RPA and BS levels for both light polarizations with the ϵ_M as reported in two experimental studies in Refs. 6 and 9. In the latter studies, ϵ_M was deduced from Kramers–Kronig analysis of the VUV reflectivity spectra discussed in the previous subsection.

The optical absorption spectra, ϵ_2, obtained from both experiments display a very steep onset that leads to a pronounced cusp at about 9 eV in correspondence with the sharp peak observed in the reflectivity. The intensity of the optical spectra then increases, leading to a strong peak in the range of 12–14 eV, whose exact location depends on the experiment and light polarization. Beyond this peak, for perpendicular light polarization the intensity falls off with a distinct shoulder-like feature at 18 eV and attains finally very low values at 25 eV and beyond. Instead for parallel light polarization the spectrum exhibits a bimodal shape with a second equally intense peak at about 18 eV before falling off in intensity for higher energies. For the perpendicular light polarization the differences between the two experimental curves is much more pronounced than for the original reflectivity data (Fig. 4). Noticeable differences exist in both peak positions and intensity, with the curves from Ref. 6 exhibiting a shift toward higher energies.

The real part, ϵ_1, shows again the sharp peak at about 9 eV followed by a second broader structure at 12–13 eV, stronger for the parallel light polarization. Eventually, the curves decrease to values close to zero, exhibiting a shoulder-like structure in the 15–16-eV range and becoming negative at about 18 eV until 25 eV. The zero crossing at about 25 eV

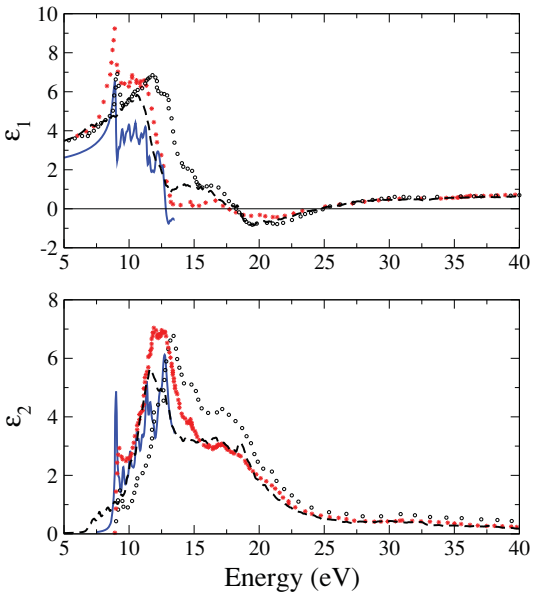

FIG. 5. (Color online) Real part, ϵ_1, and imaginary part, ϵ_2, of the macroscopic dielectric function, ϵ_M, for light polarization perpendicular to the c axis. The calculated RPA (black dashed) and BS (solid blue) curves are compared with experimental data from Ref. 6 (black circles) and Ref. 9 (red stars).

signals the excitation of a plasmon mode and will be discussed in more detail later on. For the ϵ_1 curve from Ref. 9 a near-crossing of the zero is also seen at 15 eV.

Our results agree closely with the curves from Ref. 9. For perpendicular polarization the BS results for lower energies reproduce well the experiment. In particular the peak at about 9 eV in ϵ_2 is reproduced at only the BS level, similar to the

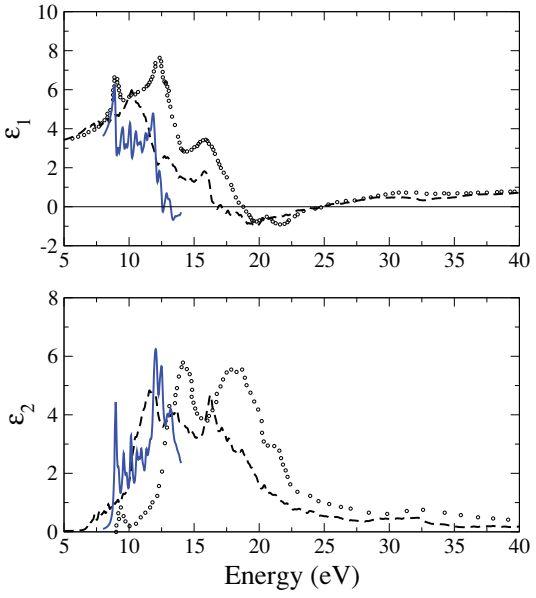

FIG. 6. (Color online) Real part, ϵ_1, and imaginary part, ϵ_2, of the macroscopic dielectric function, ϵ_M, for light polarization parallel to the c axis. The calculated RPA (black dashed) and BS (solid blue) curves are compared with experimental data from Ref. 6 (black circles).

reflectivity calculations, reaffirming its excitonic origin. The only drawback of the BS results is their predicted intensity of ϵ_1 which is strongly underestimated, a consequence of the poor convergence with respect to the number of bands (see Sec. II B). The RPA, on the other hand, reproduces the low-energy magnitude of ϵ_1. At lower energies (2 eV) the magnitude of ϵ_1 from RPA is equal to 3.15 and 3.11 for perpendicular and parallel polarizations, respectively. These values are marginally higher than the high-frequency dielectric constants ϵ_∞ obtained from spectroscopic ellipsometry data.[50,51] However, compared with experiment, the RPA displays a far more gradual increase in intensity in ϵ_2 for low energies missing completely the strong onset of oscillator strength associated with the excitonic peak. For higher energies the RPA captures well the line shape of ϵ_2 as obtained in Ref. 9 and the position of the zeros of the experimental ϵ_1 at 25 eV.

For the parallel light polarization the differences between the experimental (from Ref. 6) and calculated curves are rather pronounced. These differences are quite unexpected considering the very good agreement we obtained for the reflectivity both at low energies within the BS and at higher energies within the RPA.

The index of refraction n and extinction coefficient κ (Figs. 7 and 8) show features similar to ϵ_1 and ϵ_2, respectively, although for these dielectric functions the differences between the two experimental curves, and the experimental and theoretical curves are less pronounced. In particular, for perpendicular polarization there is a very good agreement between the experimental index of refraction and extinction coefficient from Ref. 9 and the BS results (for energies below 14 eV) and RPA results (for energies above 15 eV).

Finally, Figs. 9 and 10 compare the calculated and experimental electron energy-loss function $-\mathrm{Im}[\varepsilon_M^{-1}(\mathbf{q})]$ in the vanishing $\mathbf{q}$ limit. Again, the experimental curves were deduced from Kramers–Kronig analysis of the VUV reflectivity spectra. The only exception is for the case of perpendicular $\mathbf{q}$ orientation, where the energy-loss function obtained from electron energy-loss spectroscopy[9] (EELS) is also shown. It can be seen that for this polarization the intensity of the dominant peak varies, depending on the experiment, from 1.3 to 2. This difference in the loss functions obtained through the EELS or the VUV spectra (from Ref. 9) has been attributed to the uncertainty in the EELS due to the zero-loss extraction. On the other hand, the differences between the two loss functions

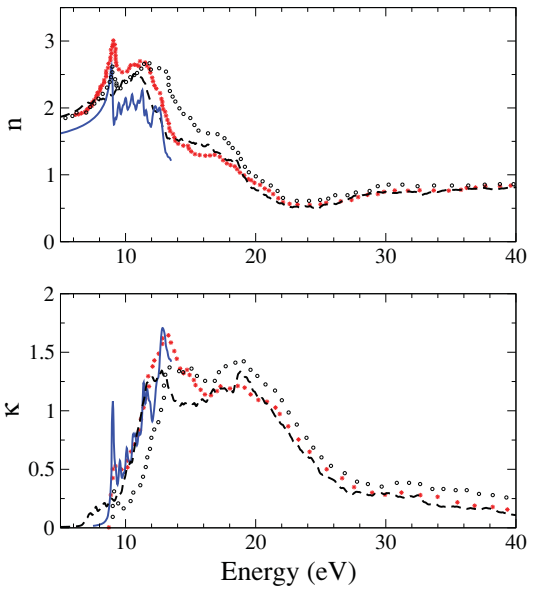

FIG. 7. (Color online) Index of refraction n and extinction coefficient κ for light polarization perpendicular to the c axis. The calculated RPA (black dashed) and BS (solid blue) curves are compared with experimental data from Ref. 6 (black circles) and Ref. 9 (red stars).

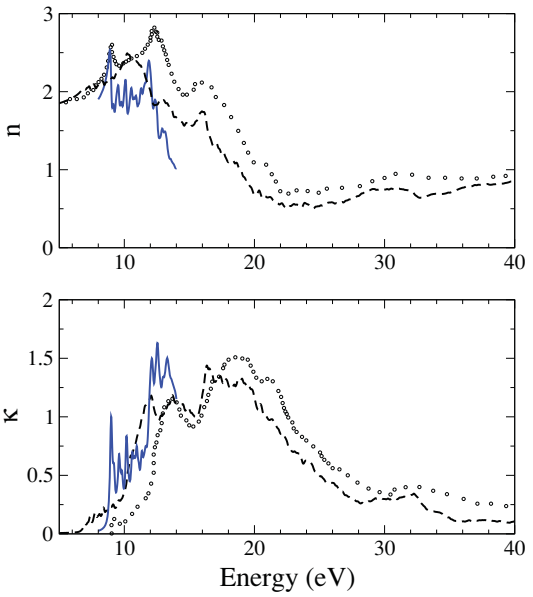

FIG. 8. (Color online) Index of refraction n and extinction coefficient κ for light polarization parallel to the c axis. The calculated RPA (black dashed) and BS (solid blue) curves are compared with experimental data from Ref. 6 (black circles).

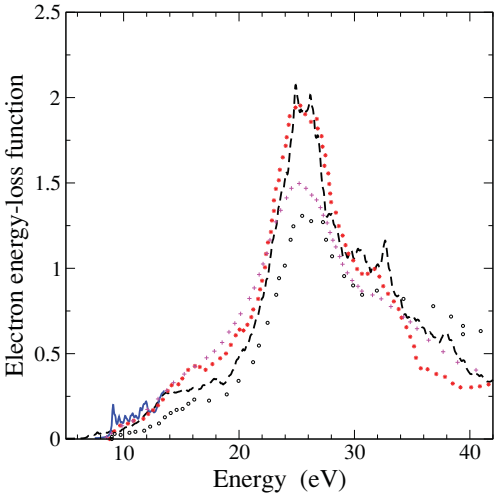

FIG. 9. (Color online) Electron energy-loss function in the vanishing $\mathbf{q}$ limit for $\mathbf{q}$ oriented perpendicular to the c axis. The calculated RPA (black dashed) and BS (solid blue) curves are compared with experimental data obtained from Kramers–Kronig analysis of VUV reflectivity spectra from Ref. 6 (black circles) and from Ref. 9 (red stars), and with experimental data from electron energy-loss spectra from Ref. 9 (magenta plusses).

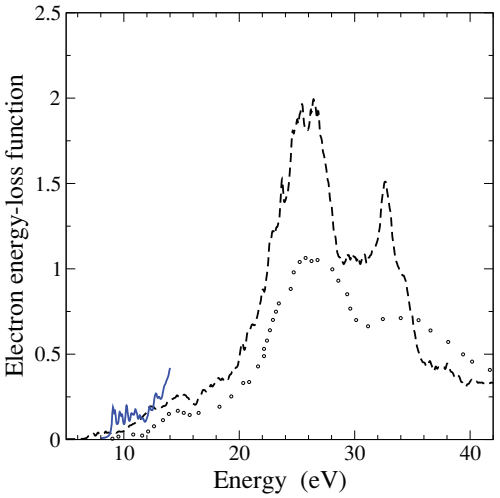

FIG. 10. (Color online) Electron energy-loss function in the vanishing **q** limit for **q** oriented parallel to the c axis. The calculated RPA (black dashed) and BS (solid blue) curves are compared with experimental data obtained from Kramers-Kronig analysis of VUV reflectivity spectra from Ref. 6 (black circles).

derived from the two different VUV reflectivity experiments instead stem directly from the details of the Kramers–Kronig analyses that use measured intensities for energies higher than 120 eV (as discussed in Ref. 9) and can affect the absolute scale of the loss functions.

The experimental curves have an onset at about 9.0 eV. For perpendicular **q** orientation both loss functions obtained from the VUV data present a shoulder at 16 eV, which is absent in the loss function obtained from the EELS measurements, a consequence of the better resolution of the VUV measurements. This feature must probably have a strong collective character, namely be plasmon-like, since ϵ_1 almost passes through zero at this energy (see Fig. 5) for the case of the function derived by French and co-workers.[9] Nonetheless, it is heavily damped because of the still large magnitude of ϵ_2 at this energy range (see Fig. 5). A similar shoulder is seen at 15 eV for the parallel **q** orientation but in this case it does not correspond to a zero crossing of ϵ_1 (Fig. 6).

At higher energies, the very intense and broad bulk plasmon appears, centered at 25.5 to 26 eV. This excitation mode represents the collective excitations of all the valence electrons of α-alumina, with its position almost coinciding with the zero of ϵ_1 (Figs. 5 and 6). Finally, another distinct shoulder-like feature also appears in the 32–34-eV region in the loss functions with a relative intensity more pronounced for the parallel polarization.

Our calculated RPA curves, again similar as in ϵ_2, underestimate the onset of the loss functions. Nonetheless, the RPA reproduces the experimental loss functions for a very extended range of energies. The agreement again is best with the function from Ref. 9 in terms of the obtained intensity. More specifically, the position of the major experimental features are reproduced and in particular the intensity, shape, and position of the dominant plasmon resonance peak. Concerning the comparison with the curves obtained from Ref. 6 the agreement is also qualitatively acceptable regarding the position of the major features of the loss function and taking into account the fact that the plasmon resonance and the overall intensities of the loss functions derived in Ref. 6 are more damped, as discussed before.

The BS results in Figs. 9 and 10 reproduce the experimental onset for either **q** orientation and provide a very good description of the intensity of the loss function obtained in Ref. 9 for the perpendicular orientation.

IV. DISCUSSION AND CONCLUSIONS

From the present results we can distinguish two energy regions for the optical response of α-alumina: The first region spans the energies from the absorption onset up to approximately 15 eV and contains the exciton and the initial part of interband transitions. The second region starts from 15 eV and contains the remaining interband transitions (originating from both I and II manifolds) together with the collective bulk plasmon resonance.

More specifically, the region up to 15 eV involves transitions from the upper valence manifold (labeled II in Fig. 1) that has mainly O($2p$) character (see Fig. 2), to the conduction bands closer to the band edge. To describe qualitatively and quantitatively the optical response in this region it is necessary to go beyond the IP level of approximation and introduce many-body effects, both QP corrections and the electron-hole attraction. The QP corrections are needed to give the correct onset, whereas the electron-hole attraction introduced at the BS level is needed to obtain the sharp peak at 9 eV that has excitonic origin. Recalculating the spectra by performing exact diagonalization of the BS equation[52] reveals that the peak at 9 eV contains two doubly degenerate excitations, at 9.0 eV (stronger) and at 9.25 eV (weaker). Analysis of these excitations in terms of independent electron-hole pairs showed that the main contribution to the intensity comes from transitions from the three upper valence bands to the lowest conduction band at Γ, although additional contributions from k points close to Γ are fundamental to obtaining a converged final position and intensity. Furthermore, by studying the intensity of the exciton peak with respect to the number of transitions we found that, although transitions between the band edges have the largest weight, transitions from other bands have to be included to converge the peak intensity. In particular we needed to include transitions from 12 valence to 12 conduction bands. Similarly, the transitions involving these bands are the dominant ones leading to converged interband peaks in ϵ_2 calculated at the BS level up to 13.5 eV (Figs. 5 and 6).

By comparing the QP gap found from the GW calculations with the energy of the lowest excitation determined by solving the BS equation, we found a binding energy for the exciton of about 0.4 eV, in agreement with the value of about 0.3 eV deduced by comparing experimental band gap and exciton positions, but larger than the value of 0.13 eV determined in Ref. 7 from analysis of temperature-dependent reflectivity data.

The region beyond 15 eV involves transitions from the full upper valence manifold (all 18 bands of it) to higher-energy conduction states and, for energies above 30 eV, as well from the lower valence manifold (labeled I in Fig. 1) that has mainly O($2s$) character (see Fig. 2). It corresponds approximately to the region in which ϵ_1 is very small. In this region, and in

particular when ϵ_1 is negative, LFEs are very strong, while QP corrections and the electron-hole attraction do not seem to be essential, since we obtain good results already at the RPA level. This is consistent with the fact that, as discussed in Ref. 6, the dielectric response in this energy range resembles that of an electron gas under a longitudinal perturbation.

Concerning the comparison with experiment, quite unexpectedly the agreement depends markedly on the specific optical function or spectrum. Whereas a very good agreement is obtained with the VUV reflectivity data from Ref. 5, the agreement is not that good for the derived dielectric functions, especially for the macroscopic dielectric function for parallel light polarization. In contrast, our results compare very favorably with the VUV reflectivity data of French and co-workers[9] as well as with their derived dielectric functions for perpendicular light polarization (see Figs. 5, 7, and 9). The reason for these differences may be due to compensation of errors in the calculated reflectivity spectra [Eq. (8)]. On the other hand it can be due to experimental uncertainties. In Ref. 9 the authors show that small differences in the reflectivity spectra, due to sample preparation and annealing treatments, are amplified in the complex macroscopic dielectric function. Furthermore, as discussed by the same authors, the Kramers–Kronig transformations may also introduce errors in the predicted dielectric functions. Our calculated macroscopic dielectric functions may help to interpret the differences in the functions derived by Kramers–Kronig analyses of reflectivity or energy-loss spectra measured for different sets of samples.

To summarize, by carrying out first-principles calculations at the RPA and GW+BS levels we reproduced quantitatively the main features of the reflectivity spectra and dielectric response functions of α-alumina. We found that incorporation of many-body effects beyond the IP approximation is imperative for a quantitative description of the optical response, with excitonic effects dominating below 15 eV and LFEs appearing noticeably at higher energies.

ACKNOWLEDGMENTS

This work was supported by the program COMPETE: FCOMP-01-0124-FEDER-010450 and by the Portuguese Fundação para a Ciência e a Tecnologia (FCT) under the Ciência 2007, 2008 and PTDC/FIS/102722/2008 programs. The computer resources of the Department of Physics of the University of Coimbra were used, including the Milipeia cluster at the Laboratory for Advanced Computing. The authors thank Fernando Nogueira and Francisco Gil for fruitful discussions and Andrea Marini for his suggestions on some of the computational aspects of the work.

[1] E. Dörre and H. Hübner, *Alumina: Processing, Properties, and Applications* (Springer-Verlag, Berlin, 1984).
[2] E. T. Arakawa and M. W. Williams, J. Phys. Chem. Solids **29**, 735 (1968).
[3] M. L. Bortz and R. H. French, Appl. Phys. Lett. **55**, 1955 (1989).
[4] R. H. French, J. Am. Ceram. Soc. **73**, 477 (1990).
[5] T. Tomiki, Y. Ganaha, T. Shikenbaru, T. Futemma, M. Yuri, Y. Aiura, S. Sato, H. Fukutani, H. Kato, T. Miyahara *et al.*, J. Phys. Soc. Jpn. **62**, 573 (1993).
[6] T. Tomiki, Y. Ganaha, T. Futemma, T. Shikenbaru, Y. Aiura, M. Yuri, S. Sato, H. Fukutani, H. Kato, T. Miyahara *et al.*, J. Phys. Soc. Jpn. **62**, 1372 (1993).
[7] R. H. French, D. J. Jones, and S. Loughin, J. Am. Ceram. Soc. **77**, 412 (1994).
[8] H. Müllejans and R. H. French, J. Phys. D **29**, 1751 (1996).
[9] R. H. French, H. Müllejans, and D. J. Jones, J. Am. Ceram. Soc. **81**, 2549 (1998).
[10] G. Dräger and J. A. Leiro, Phys. Rev. B **41**, 12919 (1990).
[11] W. L. O'Brien, J. Jia, Q. Y. Dong, T. A. Callcott, K. E. Miyano, D. L. Ederer, D. R. Mueller, and C. C. Kao, Phys. Rev. B **47**, 140 (1993).
[12] J. Olivier and R. Poirier, Surf. Sci. **105**, 347 (1981).
[13] M. H. Reilly, J. Phys. Chem. Solids **31**, 1041 (1970).
[14] R. A. Evarestov, A. N. Ermoshkin, and V. A. Lovchikov, Phys. Status Solidi B **99**, 387 (1980).
[15] I. P. Batra, J. Phys. C **15**, 5399 (1982).
[16] S. Ciraci and I. P. Batra, Phys. Rev. B **28**, 982 (1983).
[17] Y. N. Xu and W. Y. Ching, Phys. Rev. B **43**, 4461 (1991).
[18] W. Y. Ching and Y.-N. Xu, J. Am. Ceram. Soc. **77**, 404 (1994).
[19] B. Holm, R. Ahuja, Y. Yourdshahyan, B. Johansson, and B. I. Lundqvist, Phys. Rev. B **59**, 12777 (1999).
[20] P. Hohenberg and W. Kohn, Phys. Rev. **136**, B864 (1964).
[21] W. Kohn and L. J. Sham, Phys. Rev. **140**, A1133 (1965).
[22] R. Ahuja, J. M. Osorio-Guillen, J. Souza de Almeida, B. Holm, W. Y. Ching, and B. Johansson, J. Phys. Condens. Matter **16**, 2891 (2004).
[23] S. M. Hosseini, H. A. R. Aliabad, and A. Kompany, Eur. Phys. J. B **43**, 439 (2005).
[24] G. Onida, L. Reining, and A. Rubio, Rev. Mod. Phys. **74**, 601 (2002).
[25] F. Aryasetiawan and O. Gunnarsson, Rep. Prog. Phys. **61**, 237 (1998).
[26] W. G. Aulbur, L. Jonsson, and J. W. Wilkins, Solid State Phys. **54**, 1 (2000).
[27] E. E. Salpeter and H. A. Bethe, Phys. Rev. **84**, 1232 (1951).
[28] L. Hedin, Phys. Rev. **139**, A796 (1965).
[29] A. G. Marinopoulos, L. Reining, V. Olevano, and A. Rubio, Phys. Rev. Lett. **89**, 076402 (2002).
[30] L. K. Dash, N. Vast, P. Baranek, M. C. Cheynet, and L. Reining, Phys. Rev. B **70**, 245116 (2004).
[31] L. Hedin and S. Lundqvist, *Solid State Physics*, Vol. 23 (Academic, New York, 1969).
[32] R. W. Godby and R. J. Needs, Phys. Rev. Lett. **62**, 1169 (1989).
[33] M. Grüning, A. Marini, and X. Gonze, Nano Lett. **9**, 2820 (2009).
[34] V. Olevano and L. Reining, Phys. Rev. Lett. **86**, 5962 (2001).
[35] D. M. Ceperley and B. J. Alder, Phys. Rev. Lett. **45**, 566 (1980).
[36] X. Gonze, B. Amadon, P. M. Anglade, J. M. Beuken, F. Bottin, P. Boulanger, F. Bruneval, D. Caliste, R. Caracas, M. Cote *et al.*, Comput. Phys. Commun. **180**, 2582 (2009).

[37]X. Gonze, J. M. Beuken, R. Caracas, F. Detraux, M. Fuchs, G. M. Rignanese, L. Sindic, M. Verstraete, G. Zerah, F. Jollet *et al.*, Comput. Mater. Sci. **25**, 478 (2002).

[38]X. Gonze, G. M. Rignanese, M. Verstraete, J. M. Beuken, Y. Pouillon, R. Caracas, F. Jollet, M. Torrent, G. Zerah, M. Mikami *et al.*, Z. Kristallogr. **220**, 558 (2005).

[39]N. Troullier and J. L. Martins, Phys. Rev. B **43**, 1993 (1991).

[40]H. Monkhorst and J. Pack, Phys. Rev. B **13**, 5188 (1976).

[41]A. A. Mostofi, J. R. Yates, Y.-S. Lee, I. Souza, D. Vanderbilt, and N. Marzari, Comput. Phys. Commun. **178**, 685 (2008).

[42]A. Marini, C. Hogan, M. Grüning, and D. Varsano, Comput. Phys. Commun. **180**, 1392 (2009).

[43]W. Duan, R. M. Wentzcovitch, and K. T. Thomson, Phys. Rev. B **57**, 10363 (1998).

[44]A. G. Marinopoulos and C. Elsässer, Acta Mater. **48**, 4375 (2000).

[45]R. E. Newnham and Y. M. DeHaan, Z. Kristallogr. **117**, 235 (1962).

[46]N. Marzari and D. Vanderbilt, Phys. Rev. B **56**, 12847 (1997).

[47]More precisely, the fit gives a coefficient equal to 1.11 for the valence bands and 1.08 for the conduction bands. These values, together with a band-gap correction of 2.64 eV, were used to introduce the QP corrections in the BS and RPA + QP calculations.

[48]A. Kuznetsov, V. N. Abramov, V. V. Mürk, and B. P. Namozov, Sov. Phys. Solid State **33**, 1126 (1991).

[49]Also in the BS spectra the exciton peak in the reflectivity at parallel polarization is slightly lower in energy than the one in the reflectivity at perpendicular polarization, but the difference is smaller than the experimental one and also is within the acceptable error inherent in the BS calculations.

[50]A. K. Harman, S. Ninomiya, and S. Adachi, J. Appl. Phys. **76**, 8032 (1994).

[51]M. Schubert, T. E. Tiwald, and C. M. Herzinger, Phys. Rev. B **61**, 8187 (2000).

[52]To be able to perform exact diagonalization we considered only transitions between the upper five valence bands and the lowest conduction band.